RSC Advances

PAPER

View Article Online
View Journal | View Issue

Cite this: *RSC Adv.*, 2024, **14**, 19116

Crack-induced abrupt capacity degradation in commercial $LiNi_{0.8}Co_{0.1}Mn_{0.1}O_2$ (NCM811)/SiO_x-graphite pouch batteries†

Xianying Zhang,[ab] Qiyu Wang, *[ab] Yu Li,[abc] Guochen Sun,[ac] Xiqian Yu [abc] and Hong Li *[abc]

Received 6th March 2024
Accepted 29th May 2024

DOI: 10.1039/d4ra01738b

rsc.li/rsc-advances

Reasons for abrupt capacity fading in commercial $LiNi_{0.8}Co_{0.1}Mn_{0.1}O_2$ (NCM811)/SiO_x-graphite pouch batteries were evaluated using electrochemical methods. These approaches consist of charge and discharge curves, differential curves and electrochemical impedance spectroscopy (EIS), and some advanced verification techniques constituting scanning electron microscopy (SEM), X-ray photoelectron spectroscopy (XPS) and X-ray diffraction (XRD). The predominance testament concerning capacity attenuation through experimental verification after the battery is disassembled proves that the silicon-based anode material deteriorates further, bringing about a significant number of cracks with the progression of cycles. In addition, electrolyte enters into the cracks, generating the excessive growth of the solid electrolyte interface (SEI) and the expansion of impedance, which eventually causes the failure of conductive networks, dilemma of ion transmission and increment in polarization, ultimately contributing to lithium dendrites.

Introduction

Capacity degradation[1–8] is one of the most universal failure phenomena of Li-ion batteries during employment or storage. The unexpected capacity degradation, a more dreadful failure phenomenon, will generate the performance degradation of a battery and safety hazards.[9–12] Numerous investigations in terms of the fading mechanism of the capacity have been proposed, such as the structural failure of electrode materials,[6,13–17] loss of lithium inventory (LLI)[1,18,19] and active materials (LAM),[18,19] excessive growth of SEI on the surface of anodes,[3,16] and dissolution of transitional metals.[4] Nevertheless, there have been very limited investigations on the mechanisms leading to rapid capacity decay. Schuster *et al.*[20] manifested that high charging rates, ΔV (the operational voltage window), and low temperatures facilitated the emergence of nonlinear aging characteristics. Yang *et al.*[10] presented rapid aging behaviors of Li-ion cells associated with lithium plating. Yuan *et al.*[12] indicated that electrode inhomogeneity revealed the primary validation for abrupt battery degradation. However, researchers have subjected their own assembled batteries and seldom executed failure analyses on commercial cells. Therefore, we investigated the mechanism of rapid capacity decay of commercial pouch batteries.

The mechanism of the unexpected capacity degradation in $LiNi_{0.8}Co_{0.1}Mn_{0.1}O_2$ (NCM811)/SiO_x-graphite lithium-ion batteries was investigated by failure analysis technologies, incorporating diagnostic analysis and anatomical analysis. The stinging recession of the capacity happened at around 520 cycles, with 1C cycling at 25 °C. In accordance with the diagnostic inquiry, the smooth capacity decaying process variable before 520 cycles discloses the failure of materials, especially that of the silicon-based anode material. After 520 cycles, several elements promote the precipitate capacity degradation, covering the deterioration of the silicon-based anode material, growth of impedance and polarization, and loss of active lithium. The pouch batteries were disassembled at different cycle numbers. The fragments from these pouch cells were characterized by electrochemical methods and advanced measurement techniques such as SEM, XPS and XRD. Established evidence suggested that the clipping capacity degradation originated from cracks in the silicon-based anode material, deterioration of the anode material structure, overproduction of SEI, and failure of the conductive network. At the same time, all of them enhanced impedance and polarization. Subsequently, a large number of lithium dendrites were ultimately produced on the surface of the anode electrode, and the battery demonstrated an unexpected decay in capacity.

[a]*Beijing Key Laboratory for New Energy Materials and Devices, Institute of Physics, Chinese Academy of Sciences, Beijing, 100190, China. E-mail: qywang10@iphy.ac.cn*
[b]*Beijing Frontier Research Center on Clean Energy, Huairou Division, Institute of Physics, Chinese Academy of Sciences, Beijing, 101400, China*
[c]*Center of Materials Science and Optoelectronics Engineering, University of Chinese Academy of Sciences, Beijing, 100049, China*

† Electronic supplementary information (ESI) available. See DOI: https://doi.org/10.1039/d4ra01738b

Experimental

We executed electrochemical performance trials on a series of commercial 2.0 A h NCM811/SiO_x-graphite lithium-ion pouch batteries to study their rapid capacity degradation phenomenon. The anode active material was composed of graphite precursor and SiO_x powder in a weight ratio of 90/10. Anodes were prepared by mixing 94 wt% active material powder, 2 wt% super P and 4 wt% sodium polyacrylate binder. Cathodes were composed of the active material (90 wt%), polyvinylidene fluoride binder (5 wt%) and conducting carbon (5 wt%). The volumetric energy density of the batteries was calculated to be 400 W h L^{-1}.[21,22] Numerous batteries with acceptable consistency were manipulated by charge–discharge experiments optimizing L and testing devices at room temperature (25°C ± 1 °C). Next, we present the charging and discharging procedure in detail. The first step was to charge–discharge them for three cycles with a current of 0.2 A (0.1C) between 2.8 to 4.2 V in constant current (CC) mode to activate them and gain a stable voltage. The statistics of the third cycle were selected as the original data of the battery at 0.1C rate. Then, we set the charge/discharge cycle program as the constant current charging mode at 2.8–4.2 V electrochemical window, applying a current of 2 A (1C) for 19 cycles, then 0.2 A (0.1C) for 1 cycle as a cycle unit, and repeated the cycle unit. In order to ensure these batteries were sufficiently stable after charging and discharging, the resting time between each charge and discharge was 1 h.

The pouch samples were selected at specific cycled numbers according to their electrochemical performances and subsequently disassembled at 2.8 V (0% SOC (the state of charge)). After the batteries were disassembled, we selected a portion of the samples according to the distinct macroscopic phenomena on the surface of the electrode and rinsed them several times with dimethyl carbonate (DMC) in the glove box to remove the residual electrolyte on the surface of the electrode, and then dried them in a vacuum chamber for 2 h before characterization. In addition, the double-sided cathodes and anodes were wiped into single-sided ones. The single-sided electrodes were assembled into coin cells for electrochemical assessment. Surface morphologies of the electrodes were characterized by a field emission scanning electron microscope (FE-SEM, SU8010, Hitachi). The X-ray diffraction (XRD) data were obtained in the scan range (2θ) of 10–80° with an increment of 0.02° by an X-ray diffractometer, D8 Advance, Bruker (Cu Kα radiation). The Autolab electrochemical workstation accomplished the electrochemical impedance spectroscopy (EIS) evaluations with the check frequency from 10 MHz to 0.1 MHz, and the disturbance voltage was 5 mV. Similarly, the software Nova 2.1 was utilized to fit data. The XPS statistics were fetched by ESCALAB 250 Xi, Thermo Fisher applying monochromatic 150 W Al Kα radiation and evaluated with the software Advantage. At the same time, the C 1s line of carbon black at 284.4 eV was selected to calibrate binding energies. All XPS samples were transferred using a Thermo Fisher-supplied vacuum transfer cassette to ensure the accuracy of the experimental results.

Results and discussion

In order to highlight the mechanism of the precipitate capacity degradation in NCM811/SiO_x-graphite lithium-ion batteries, the cycling trials were overseen under the voltage window of 2.8–4.2 V with 1C current at 25 °C. The cycled inputs of pouch batteries at different cycle numbers are demonstrated in Fig. 1(a). It reveals that the capacity of the fresh pouch battery is 1.471 A h in the 1st cycle using a current of 2 A (1C). The capacity remains at 1.176 A h (capacity retention of 79.95%) undergoing 440 cycles, and the coulombic efficiency remains stable throughout the process (Fig. 1(b)). By comparison, the coulombic efficiency changes apparently after ~450 cycles. The capacity retention abruptly decays to 21.21% during the 440–620 cycles, and the phenomenon of abrupt capacity degradation emerges. In agreement with the testimonies on the degradation rate (Fig. 1(c)), the highest degradation rate indicated approximately 12 mA h per cycle during 520–560 cycles. Hence, the unexpected capacity degradation materializes at about the 500th cycle, and the high degradation rate maintains during 500–580 cycles.

The electrochemical property was monitored for diagnostic analysis to investigate the underlying arguments for the abrupt capacity degradation. The charge and discharge curves of the pouch batteries optimizing a current of 0.1C at 25 °C for contrasting cycles under the voltage window of 2.8–4.2 V are illustrated in Fig. 2(a). The original capacity of the battery indicates 2.075 A h from the curves, and the capacity of the battery is 1.834 A h at 440 cycles. As a result, the capacity retention ratio during this process is 88.39%. As mentioned above, the capacity retention ratio revealed 79.95% when cycled to 440 cycles with 1C current, so the percentage of capacity loss in this process due mainly to polarization suggests approximately 8.44%, and further calculations are needed to confirm the specific data. Furthermore, as cycling progresses, the battery's initial charging voltage rises from 3.2 V to 3.8 V, signifying the increase in internal resistance and polarization.[5] The polarization phenomenon of the battery was also evaluated, and the outcomes are presented in Fig. 2(b). The percentage of capacity loss due to polarization in 521 and 621 cycles is 10.84% and 48.50% [the change of polarization ratio $= (1 - C_{1C,n-1}/C_{0.1C,n}) - (1 - C_{1C,original}/C_{0.1C,original})$, where $C_{1C,n-1}$ and $C_{0.1C,n}$ represent the capacity of 1C at $(n-1)$ cycles and the capacity of 0.1C at n cycles], respectively. It demonstrates that increasing polarization proves a significant validation inducing the rapid attenuation of the capacity at 1C, especially after 500 cycles. It is speculated that the testaments for soaring polarization are related to the growth of the interface layer (SEI layer) and the damage of material particles. Based on the cycle variation curves (Fig. 2(a)), differential curves of capacity, *i.e.*, incremental capacity (IC) curves (Fig. 2(c)) and differential voltage (DV) curves (Fig. 2(d)), were accessed by differential processing of 0.1C cycle testimony for further investigation. During the process of charging, the delithiated SiO_x-graphite anode material undergoes five distinct phase transition processes labeled ❶–❷ and established in Fig. 2(c).[23] The ❶ and ❷ are the

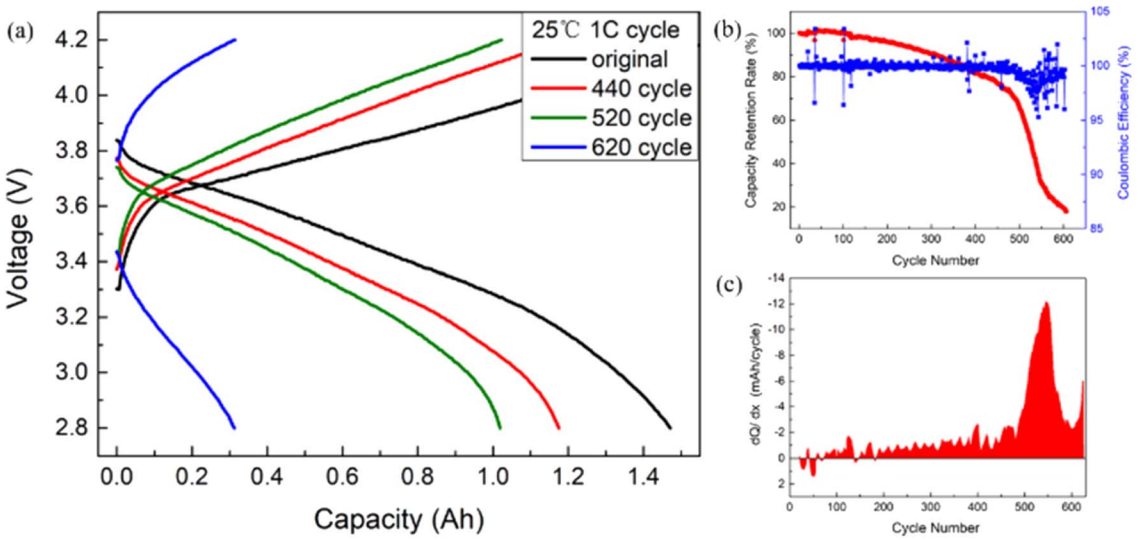

Fig. 1 (a) The charge–discharge curves of the pouch battery at different cycles (25 °C/1C), (b) the capacity retention rate and coulombic efficiency and (c) the degradation rate curve.

delithiated peaks of graphite, while ❸, ❹ and ❺ represent the delithiated behavior of SiO_x.[23] ①and ② represent the solid solution and phase transformation in the cathode material NCM811, respectively.[24] The phase transformation processes represented by peaks ❺*②, ❷*② and ❶*② are the original layered structure (H_1) being transformed into monoclinic phase (M), monoclinic phase (M) being transitioned into hexagonal phase (H_2), and finishing into hexagonal phases (H_3), respectively.[6] The phase transformation in the cathode material NCM811 could be attributed to the exchange between Ni^{2+} and Ni^{4+} when lithium ions are inserted and disinserted.[6] The peak position ❶*② has no significant variation from the original

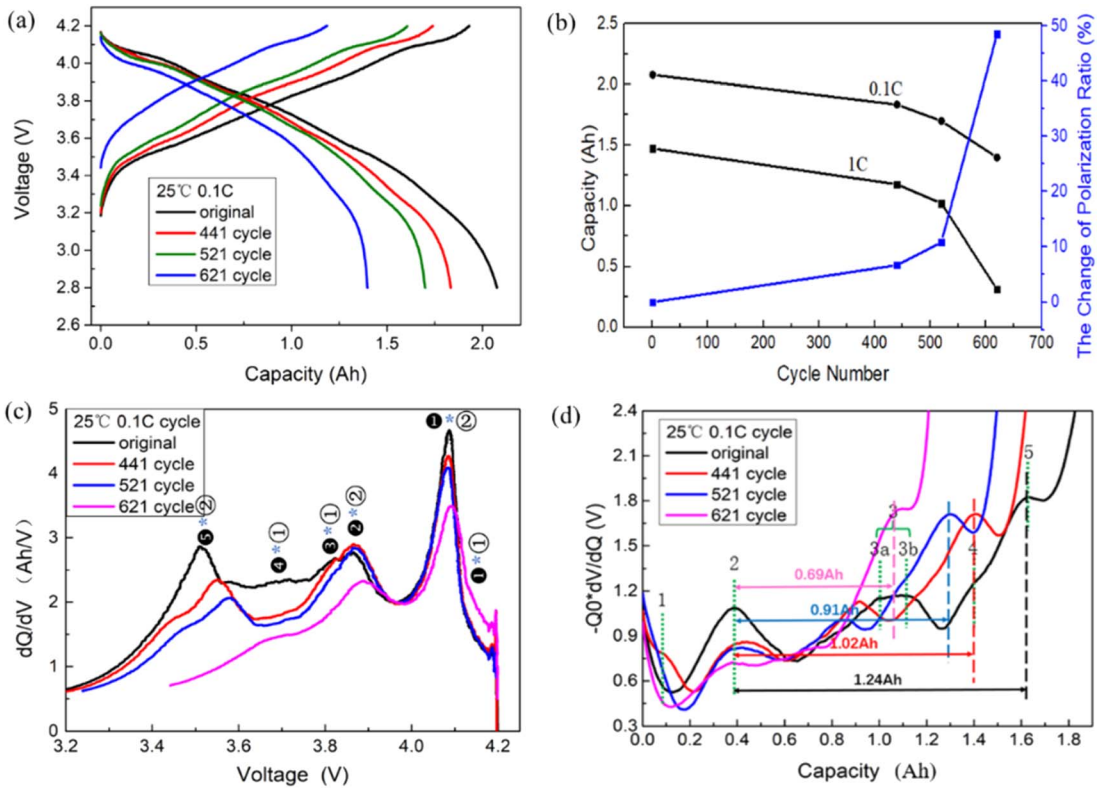

Fig. 2 (a) The charge and discharge curves of pouch batteries at room temperature (0.1C), (b) the polarization curve of pouch batteries, the corresponding differential curves of the charge and discharge cycles (0.1C), (c) IC curves and (d) DV curves.

cycle (0.1C) to the 521th cycle. However, there is a noticeable revolution toward higher voltages in the range from 521 to 621 cycles, which is presumed to be related to the irreversible phase transition of the cathode material. At the same time, the notable decline in the peak intensity ❶*②, especially during the 521–621 cycles, indicates the dropping in the precipitation potential of lithium, so it is presumed that there may be lithium plating after 521 cycles. The peak positions below 3.8 V (including ❸*①, ❹*① and ❺*②) transfer to the high potential, demonstrating the emergence of unmistakable lithium contraction. During the whole process, the innovations of ❹*① and ❺*② were the most distinguished, establishing that reductions of anode active materials and the active lithium inventory were predominant variables.[25] The alteration of peak position to high potential confirms that the advance of internal impedance may be due to the formation and thickening of SEI accompanied by the loss of active lithium.[26] Differential voltage (DV) analysis is an adequate approach for determining how much capacity different materials provide depending on adjustments in the horizontal coordinate of the peak position. There are five peaks in the DV curves in Fig. 2(d), where peak 1 derives from the cathode, peak 2 originates from the combination of cathode and anode but primarily anode, and peaks 3–5 hail from the anode.[27] Fig. 2(d) confirms a conspicuous modification in the whole cycle with peaks 2–5. The shrinkage in intensity of peak 2 establishes the presence of side reactions throughout the process and the possible formation of SEI. However, the most indisputable variation is the distance between peaks 2 and 5. The distance between peaks 2 and 5 diminishes dramatically as the cycle progresses, illustrating that the active material, particularly anode materials, is disoriented during the process.[28] From Fig. 2(d), it can be revealed that the distances between peaks 2 and 5 at the original cycle (0.1C) and the 621th cycle are 1.24 A h and 0.69 A h, respectively, with a capacity degradation of 0.55 A h. By the charge/discharge curve of 0.1C, Fig. 2(a) shows that the capacity loss of the whole battery at the cycle to 621 cycles is 0.677 A h. Therefore, the loss percentage of the pouch battery capacity associated with the anode is approximately 81.24%. In other words, the anode is the predominant confirmation of precipitate battery capacity degradation.

Electrochemical impedance spectroscopy (EIS) is another important diagnostic tool for batteries. Fig. 3 shows that the impedance of the batteries increases as the cycle goes on. The valuation of Rb (the real part of the impedance at zero crossing) ranges from 44.004 mΩ to 63.971 mΩ in cycles 441 to 641, disclosing the presence of electrolyte depletion and microcrack formation in the particle during this process.[29] At the same time, the R_{sei} (the resistance associated with SEI) goes from 7.297 mΩ to 26.03 mΩ, confirming that there is also a large amount of electrolyte decomposed to produce the interfacial layer SEI. As the anode surface SEI grows, the coating on the surface of the anode thickens, which provokes an increase in R_{ct} (the resistance associated with charge transfer). It can be concluded that the formation of microcracks in the particles precipitates large consumption of electrolytes and the excessive growth of the SEI layer, thus generating the disruption of the conducting network and the rapid increment of impedance. Combined with the foregoing analysis, it is speculated that microcracks are principally produced on the silicon-based anode material.

The batteries are disassembled at different cycle numbers for failure analysis. Based on the diagnostic analysis, we concentrate on the electrochemical performances and structures of the materials and electrodes. The charge–discharge curves of NCM811//Li coin cells at 0.1C rate in Fig. 4(a) demonstrate that the discharge-specific capacity of the cathode electrode in the coin cells declines from 173.25 mA h g^{-1} to 159.53 mA h g^{-1} at 0.1C rate, and the loss rate is approximately 7.92%. The rate of cathode polarization was 1.59% at the 621th cycle in the inset of Fig. 4(a). Therefore, the percentage of capacity loss induced by the phase transformation of the cathode material is 6.33%.

Meanwhile, the charge–discharge curves of graphite-SiO_x//Li coin cells at different cycles are established in Fig. 4(b) at 0.1C and Fig. S6(b)† at 1C. Table 1 presents the specific capacities for 0.1C charging and discharging. The discharge-specific capacity

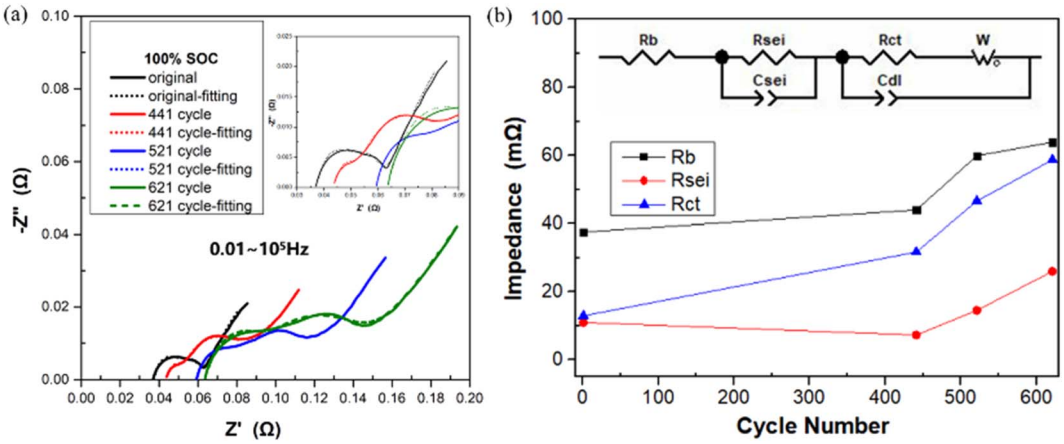

Fig. 3 EIS of the pouch batteries at 100% SOC (25 °C, 0.1C) for different cycles in (a), and the equivalent circuit model of EIS measurement and results in (b).

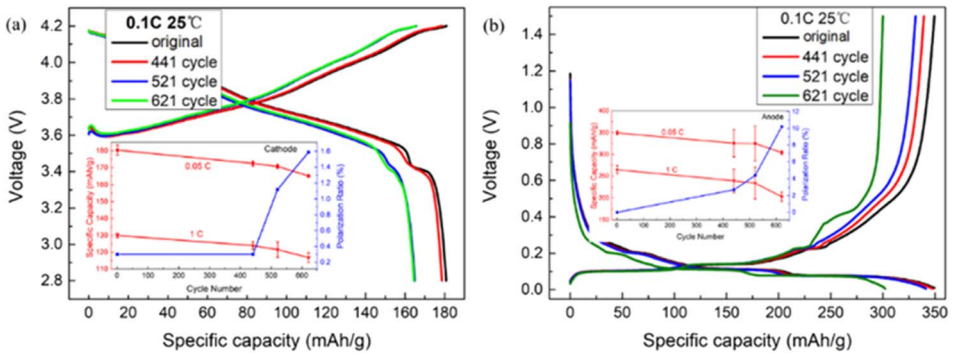

Fig. 4 The charge–discharge curves of coin cells (a) NCM811//Li and (b) graphite-SiO_x//Li at the original, 441th, 521th and 621th cycles with 0.1C at room temperature (25 °C).

Table 1 The charge and discharge specific capacities of graphite-SiO_x//Li coin cells at 0.1C

Cycle number	1	441	521	621
Charge specific capacity (mA h g^{-1})	349.48	339.45	331.40	300.01
Discharge specific capacity (mA h g^{-1})	349.42	347.68	341.50	302.33

discounts from 349.12 mA h g^{-1} to 302.33 mA h g^{-1}. The anode discharge-specific capacity of the 621th cycle in the coin cells accounts for 86.52% of the discharge capacity of the original cycle (0.2 A, 0.1C) anode electrode, instead of 67.31% (the capacity retention of the pouch battery at the 621th cycle), which affirms that the capacity loss of pouch batteries is primarily generated by reversible lithium loss and the loss rate is 19.21%. In addition, 13.48% of the capacity loss is attributed to the polarization and failures of the anode material. By comparing the anode discharge specific capacities of 0.05C and 1C in coin cells, the anode polarization rate was 10.20% at the 621th cycle (in the inset of Fig. S6(b)†). Therefore, the rate of battery capacity loss due to anode material loss is 3.28%.

In Fig. 4(b), the discharge capacity is higher than the charge capacity of the 441th and 521th cycles, which confirms the existence of reversible lithium loss on the anode material of the pouch batteries. According to the discharge curves of the coin cells in Fig. 4(b), from the original cycle (0.2 A, 0.1C) to the 521th cycle, the three charging/discharging platforms of graphite (0.08/0.1 V, 0.11/0.14 V, 0.2/0.22 V) and the charging/discharging platform of silicon-based materials are shifted to lower potential. This indicates that the loss of battery capacity is provoked by their joint action, which is also consistent with the conclusion collected from the previous DV analysis. However, in the charging curves from the 521th to 621th cycles, the hardly changed graphite platforms and the higher potential shift of silicon-based materials demonstrated that silicon-based materials chiefly led to the abrupt capacity decline of the process.

XRD characterized the structures of the cathode and anode electrodes, as shown in Fig. 5(a) & (b), respectively. Fig. 5(a) illustrates that the crystal structure of NCM is indexed to the hexagonal α-$NaFeO_2$ structure with a space group of $R\bar{3}m$, which proves that no additional peaks are generated by comparing the XRD patterns of NCM811 after various cycles, illustrating that NCM811 maintains a favorable layered structure. The consequences of the analysis of the XRD patterns for contrasting

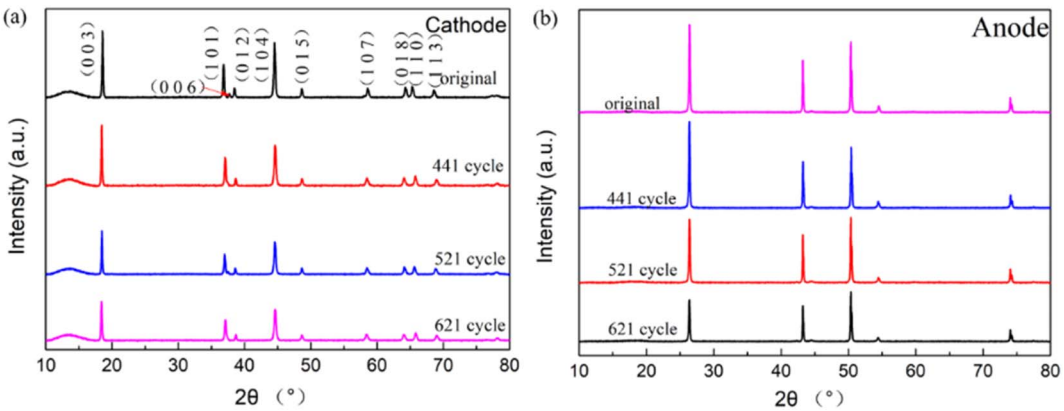

Fig. 5 XRD patterns for (a) cathode and (b) anode electrodes after different cycles.

Table 2 The results of the analysis of the XRD patterns of lithiated NCM811 for different cycles

Cycle number	Original (0.1C)	441th cycle	521th cycle	621th cycle
a (Å)	2.8547	2.8429	2.8382	2.8361
c (Å)	14.2905	14.3647	14.3992	14.4166

cycles are given in Table 2. The lattice parameter '*a*' represents the variation of the transition metal layer, and the lattice parameter '*c*' serves as the interlayer distance.[26,30] When lithium loss emerges in the NCM material, the merger of oxygen–oxygen electrostatic repulsion generates the lattice parameter '*c*'. At the same time, the further oxidation of $Ni^{2+} \rightarrow Ni^{3+} \rightarrow Ni^{4+}$ reduces the Ni ion radius, thus inducing a cutback in the lattice parameter '*a*'.[26,31] Therefore, the contraction of the lattice parameter '*a*' and the expansion of '*c*' after cycling (as shown in Table 2) are essential evidence of lithium loss in the cathode. The outcome demonstrates that some lithium ions cannot retire to the cathode material after cycling, which may be deposited on the anode material.[3,26] Fig. 5(b) manifests the crystal structure of the anode. With the progress in cycling, the intensities of the graphite peak decrease, making known that the SEI film thickens on the surface of the anode material.[26,32]

The surface morphologies of the anode are further characterized and shown in Fig. 6. We used the backscatter image (Fig. S1†) and EDX mapping (Fig. S2†) to differentiate the composition of the anode particle before morphology analysis. It demonstrates that no noticeable abnormal area is generated on the anode surface of the original cycle (0.1C), and the silicon-based particles are relatively outright. In addition, the graphite particles are comparatively uniform, with an accessible structure of the SEI film and no distinct protrusion. A thin film (about hundreds of nanometers) appears on the surface of the Si-based particle, as shown in Fig. S3.† With increasing cycle numbers (441 cycles), the cracks on the surface of silicon-based particles and the pulverization of internal structures in silicon-based particles have been arising. After 520 cycles, a small quantity of white spots appears on the anode electrode, and the SEM figure demonstrates that it boasts the dendrite structure. Combined with its conductivity and the electrode information in the batteries (no carbon nanotubes and other similar morphology materials), it is judged that the white spots in this area are lithium dendrites. The statistics can further verify that the IC figure in the above diagnostic analysis infers lithium deposition. In the sample of the 621th cycle, a sea of gray-white areas appears on the surface of the anode electrode, and it is more remarkable that these grey-white areas are lithium dendrites, as shown in Fig. 6(d). Besides, the cracks in Si-based particles can be discovered on the cross-sectional SEM (Fig. S3†) and surface SEM images (Fig. S4†), which belong to some black area of the anode sample of the 621th cycle. Compared with the original sample, the SiO_x particles of the anode sample at the 621th cycle were surrounded by cracking or pulverization and F element-based SEI covering (about several micrometers thick). It indicates that the cracking of SiO_x particles and the growth of SEI happened during the cycle.

For the sake of confirming the diversities in the chemical components of the anode surface and the radical causes of the battery capacity degradation, XPS technology[33,34] was utilized to characterize the anode surface, as shown in Fig. 7. The XPS C 1s spectra of graphite-SiO_x electrodes exhibits three prominent peaks at 284.8 eV (C–C/C–H), 286.5 eV(C–O) and 289.4 eV (CO_3).

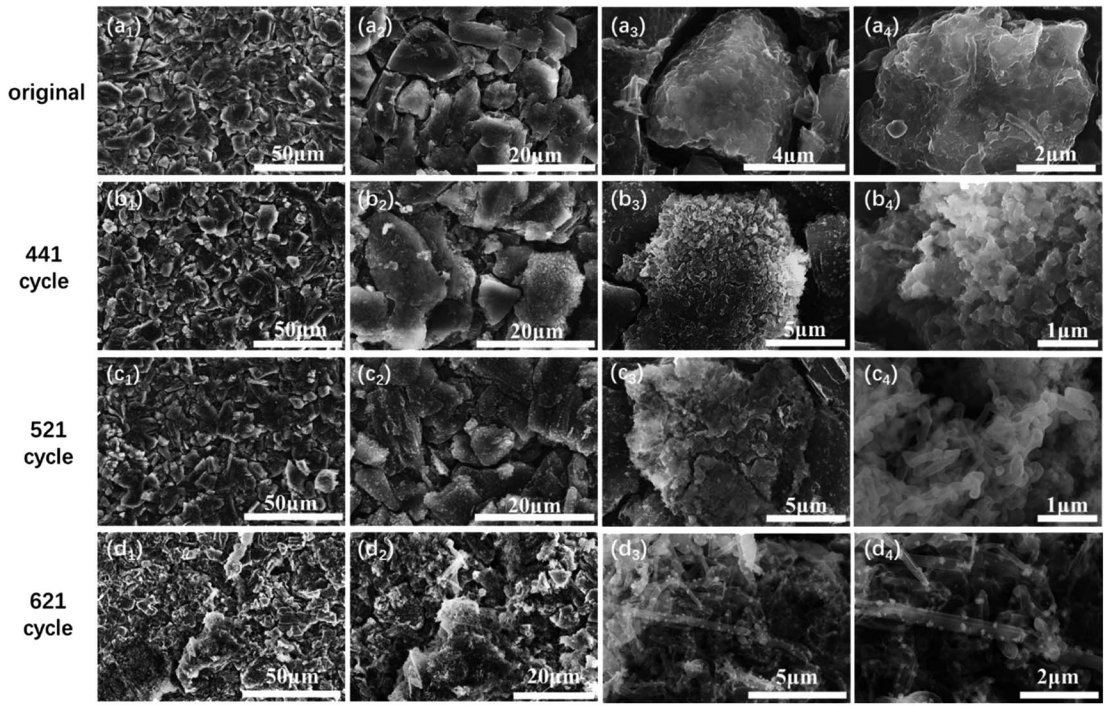

Fig. 6 SEM images of anodes after different cycles (a) original, (b) 441 cycles, (c) 521 cycles and (d) 621 cycles.

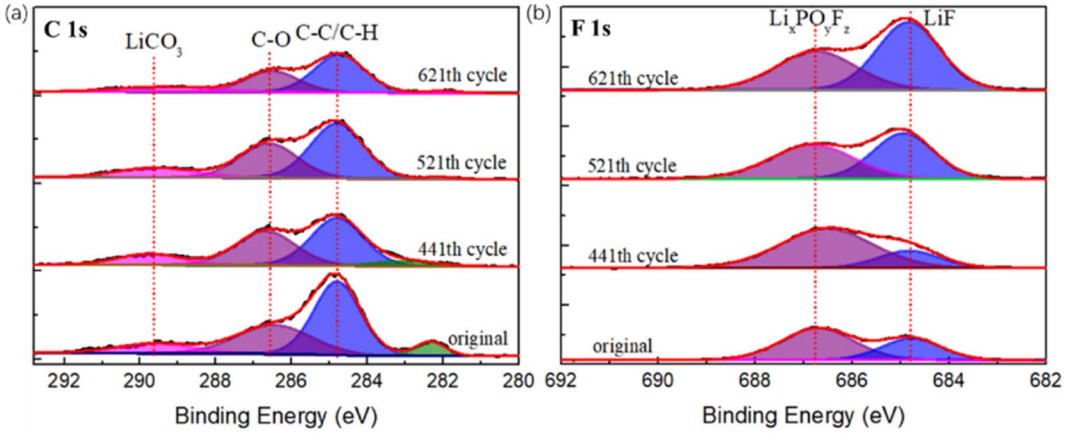

Fig. 7 XPS spectra of graphite-SiO_x electrodes from pouch batteries at the original and after 441, 521 and 621 cycles for (a) C 1s and (b) F 1s.

Along with the cycling, the peak intensities of C–C/C–H and C–O decline, which suggests the organics of SEI have attenuated. At the same time, the XPS F 1s spectra of graphite-SiO_x electrodes exhibit two main peaks, which are assigned to LiF and $Li_xPO_yF_z$. The peak intensities of LiF and $Li_xPO_yF_z$ increase along with the cycling, which illustrates that the inorganics of SEI have augmented. Therefore, it can be concluded that as the cycle proceeds, the electrolyte decomposition generates a decline in organic and an increment in inorganic on the SEI surface, provoking a thickening of the SEI film and a decrease in surface conductivity. Then, it produces a recession in battery capacity. The increased amount of LiF can be attributed to the accelerated decomposition of the electrolyte.

Conclusion

To sum up, the predominant testament for the unexpected capacity degradation of this batch of commercial pouch batteries demonstrates the cracks in the silicon-based anode electrode materials. The capacity loss rate of the whole pouch battery was 78.79% at 620 cycles, of which the capacity loss rate related to the anode was approximately 64.01% (81.24% of the total loss rate). The capacity loss rate directly caused by the anode electrode material was measured to be 13.48% utilizing coin half-cells, of which nearly 10.2% was generated by polarization and roughly 3.28% was provoked by the loss of active material (LLM). The surface anode electrode still maintains a wonderful skeleton architecture of the carbon material by XRD experiment conclusions. Therefore, it was concluded that the capacity loss associated with the anode electrode was primarily induced by the silicon-based material. At the same time, the SEM evaluation consequences also further support that cracks were generated in the anode electrode, and the cracks would establish a fresh interface to consume a large amount of electrolyte, provoking the continuous generation and thickening of SEI, which precipitated the upsurge of battery impedance, thus producing boost polarization and reversible lithium loss, and subsequently generating the rapid decay of battery capacity. The cathode electrode half-cell trial outcomes confirmed that the capacity loss rate directly induced by the cathode electrode is 7.92%, of which polarization accounted for 1.59% and phase transition occupied 6.33%. Consequently, the ultimate rate of capacity loss generated by the perfect pouch battery consists of 7.92% for cathode material, 13.48% for anode material, 19.21% for reversible lithium loss, 36.71% for cell polarization, and 1.47% for other reasons.

In conclusion, unexpected capacity degradation is due to cracks in the silicon-based material. In the procedure of lithium intercalation–deintercalation, silicon materials are prone to generating colossal stress, which induces the fracture and pulverization of the anode and generates the instability of the SEI film on the surface. Unstable SEI continuously generates fresh interfaces to consume the electrolyte further to produce SEI, precipitating electrolyte depletion and build-up of internal resistance. Eventually, an appreciable number of lithium dendrites are generated in the anode electrode, and the pouch cells experience rapid capacity degradation.

Author contributions

Zhang Xianying: investigation, validation, data analysis, writing – editing and revised draft. Wang Qiyu: conceptualization, writing – review & editing, supervision. Li Yu: investigation & characterization. Sun Guochen: investigation. Tang Ling: resources. Yu Xiqian: investigation & review. Hong Li: conceptualization, writing – review & editing, supervision.

Conflicts of interest

The authors declare that they have no known competing financial interests or personal relationships that could have appeared to influence the work reported in this paper.

Acknowledgements

This work was supported by the New Energy Vehicle Power Battery Life Cycle Testing and Verification Public Service Platform Project [grant number 2022-235-224] and Beijing Municipal Science & Technology Commission (Z221100006722015).

References

1 M. Dubarry and B. Y. Liaw, *J. Power Sources*, 2009, **194**, 541–549.
2 K. Honkura, K. Takahashi and T. Horiba, *J. Power Sources*, 2011, **196**, 10141–10147.
3 H.-R. Kim, S.-G. Woo, J.-H. Kim, W. Cho and Y.-J. Kim, *J. Electroanal. Chem.*, 2016, **782**, 168–173.
4 K. Amine, Z. Chen, Z. Zhang, J. Liu, W. Lu, Y. Qin, J. Lu, L. Curtis and Y.-K. Sun, *J. Mater. Chem.*, 2011, **21**, 17754–17759.
5 S. D. Beattie, M. J. Loveridge, M. J. Lain, S. Ferrari, B. J. Polzin, R. Bhagat and R. Dashwood, *J. Power Sources*, 2016, **302**, 426–430.
6 H.-H. Ryu, K.-J. Park, C. S. Yoon and Y.-K. Sun, *Chem. Mater.*, 2018, **30**, 1155–1163.
7 X. Bai, T. Li and Y. J. Bai, *Dalton Trans.*, 2020, **49**, 10003–10010.
8 H.-H. Ryu, B. Namkoong, J.-H. Kim, I. Belharouak, C. S. Yoon and Y.-K. Sun, *ACS Energy Lett.*, 2021, **6**, 2726–2734.
9 E. Sarasketa-Zabala, F. Aguesse, I. Villarreal, L. M. Rodriguez-Martinez, C. M. López and P. Kubiak, *J. Phys. Chem. C*, 2014, **119**, 896–906.
10 X.-G. Yang, Y. Leng, G. Zhang, S. Ge and C.-Y. Wang, *J. Power Sources*, 2017, **360**, 28–40.
11 D. Müller, T. Dufaux and K. P. Birke, *Batteries*, 2019, **5**, 49.
12 C. Yuan, H. Wang, D. Huang, C. Wu, D. Zhou and A. Mei, *Solid State Ionics*, 2022, **374**, 115832.
13 Y. W. Zeng, *J. Power Sources*, 2008, **183**, 316–324.
14 B. Song, Z. Liu, M. O. Lai and L. Lu, *Phys. Chem. Chem. Phys.*, 2012, **14**, 12875–12883.
15 S.-K. Jung, H. Gwon, J. Hong, K.-Y. Park, D.-H. Seo, H. Kim, J. Hyun, W. Yang and K. Kang, *Adv. Energy Mater.*, 2014, **4**, 1300787.
16 H. Zheng, Q. Qu, G. Zhu, G. Liu, V. S. Battaglia and H. Zheng, *ACS Appl. Mater. Interfaces*, 2017, **9**, 12445–12452.
17 Y. Ruan, X. Song, Y. Fu, C. Song and V. Battaglia, *J. Power Sources*, 2018, **400**, 539–548.
18 M. Dubarry, C. Truchot, B. Y. Liaw, K. Gering, S. Sazhin, D. Jamison and C. Michelbacher, *J. Power Sources*, 2011, **196**, 10336–10343.
19 M. Dubarry, C. Truchot and B. Y. Liaw, *J. Power Sources*, 2014, **258**, 408–419.
20 S. F. Schuster, T. Bach, E. Fleder, J. Müller, M. Brand, G. Sextl and A. Jossen, *J. Energy Storage*, 2015, **1**, 44–53.
21 P. Bhattacharya, J. H. Lee, K. K. Kar and H. S. Park, *Chem. Eng. J.*, 2019, **369**, 422–431.
22 A. Samanta Roy Choudhury, S. Kumar, N. Gupta, A. Jana and P. Bhattacharya, *ACS Appl. Electron. Mater.*, 2024, **6**, 1140–1150.
23 L. Wang, B. Zhang, J. Pang, Y. Liu, X. Wang, Z. Chang and S. Lu, *Electrochim. Acta*, 2018, **286**, 219–230.
24 S. S. Zhang, *J. Energy Chem.*, 2020, **41**, 135–141.
25 M. Dubarry, C. Truchot, M. Cugnet, B. Y. Liaw, K. Gering, S. Sazhin, D. Jamison and C. Michelbacher, *J. Power Sources*, 2011, **196**, 10328–10335.
26 L. Wang, B. Zhang, Y. Hu, X. Li and T. Zhao, *J. Power Sources*, 2021, **482**, 228978.
27 I. Bloom, J. Christophersen and K. Gering, *J. Power Sources*, 2005, **139**, 304–313.
28 I. Bloom, J. P. Christophersen, D. P. Abraham and K. L. Gering, *J. Power Sources*, 2006, **157**, 537–542.
29 W. Choi, H.-C. Shin, J. M. Kim, J.-Y. Choi and W.-S. Yoon, *J. Electrochem. Sci. Technol.*, 2020, **11**, 1–13.
30 B. Stiaszny, J. C. Ziegler, E. E. Krauß, J. P. Schmidt and E. Ivers-Tiffée, *J. Power Sources*, 2014, **251**, 439–450.
31 T. Waldmann, M. Wilka, M. Kasper, M. Fleischhammer and M. Wohlfahrt-Mehrens, *J. Power Sources*, 2014, **262**, 129–135.
32 T. Waldmann, A. Iturrondobeitia, M. Kasper, N. Ghanbari, F. Aguesse, E. Bekaert, L. Daniel, S. Genies, I. J. Gordon, M. W. Löble, E. De Vito and M. Wohlfahrt-Mehrens, *J. Electrochem. Soc.*, 2016, **163**, A2149–A2164.
33 N. Gupta, R. K. Sahu, T. Mishra and P. Bhattacharya, *J. Mater. Chem. A*, 2022, **10**, 15794–15810.
34 N. Gupta and P. Bhattacharya, *J. Mater. Chem. C*, 2023, **11**, 13503–13517.